# Squigraphs for Fine and Compact Modeling of 3-D Shapes

Djamila Aouada, *Member, IEEE*, and Hamid Krim, *Fellow, IEEE*

***Abstract*—We propose to superpose global topological and local geometric 3-D shape descriptors in order to define one compact and discriminative representation for a 3-D object. While a number of available 3-D shape modeling techniques yield satisfactory object classification rates, there is still a need for a refined and efficient identification/recognition of objects among the same class. In this paper, we use Morse theory in a two-phase approach. To ensure the invariance of the final representation to isometric transforms, we choose the Morse function to be a simple and intrinsic global geodesic function defined on the surface of a 3-D object. The first phase is a coarse representation through a reduced topological Reeb graph. We use it for a meaningful decomposition of shapes into primitives. During the second phase, we add detailed geometric information by tracking the evolution of Morse function's level curves along each primitive. We then embed the manifold of these curves into $\mathbb{R}^3$, and obtain a single curve. By combining phase one and two, we build new graphs rich in topological and geometric information that we refer to as squigraphs. Our experiments show that squigraphs are more general than existing techniques. They achieve similar classification rates to those achieved by classical shape descriptors. Their performance, however, becomes clearly superior when finer classification and identification operations are targeted. Indeed, while other techniques see their performances dropping, squigraphs maintain a performance rate of the order of 97%.**

***Index Terms*—Iso-geodesic curves, object matching, Reeb graph, shape geometry, topo-geometric modeling, Whitney embedding.**

## I. Introduction

As a result of a fast development of 3-D data rendering and acquisition techniques, applications of 3-D modeling (e.g., security, multimedia, biometrics) have, over the last decade, received a great deal of attention from both the scientific and the engineering communities. Important efforts aim to achieve simpler representations of 3-D objects in order to efficiently carry out operations such as object classification, recognition, identification and retrieval, with acceptable error rates. Numerous 3-D representation approaches have recently been proposed, as overviewed in [1] and [2]. In the present work, we propose a 3-D object representation model that offers different levels of discrimination. This model invokes an object's geometric and topological information. This rather recent technique, henceforth referred to as *topo-geometric modeling* of 3-D objects, was first exploited in [3], where Yu *et al.* simultaneously define topological and geometrical feature maps. They show that these feature maps are invariant to all affine transforms. This invariance includes, by definition, non uniform scaling transforms. This, in turn, implies an inaccurate dissimilarity measure between the geometry of shapes, as the geometry of shapes is only invariant to Euclidean transforms. Tung and Schmitt [4] and Baloch *et al.* [5] present a different theme by first representing the topology of a 3-D shape, and subsequently enhancing with its geometrical representation. The advantage of separating the modeling into two distinct steps is twofold: First it provides two levels of discrimination; a) a coarse level with a simple topological skeleton called a *Reeb* graph [6], [7], and b) a fine level with geometric weights assigned to each edge or node of the previously extracted topological graph. Another advantage of a topological graph representation of an object is its ability of matching objects by parts, thereby enabling a transition from a global to a localized correspondence between shapes (e.g., mechanical parts, manufactured solids). In representing an object, one ideally avoids choosing a reference point extrinsic to its surface [11]–[14]. To that end, we address this limitation, evident in [3], [5], by adopting an integrated geodesic distance function as defined in [11]. Such a function ensures the invariance of the Reeb graph of an object subjected to any isometric transform. As first proposed in [11], this function was limited to only providing topological information of an object surface. Tung and Schmitt [4], in an attempt to mitigate this limitation, proposed to revert back to a Euclidean reference frame to compute differential geometric features which they use as weight attributes on the Reeb graph. In this paper, we propose a novel alternative technique that is efficient, theoretically sound, practically complete, and computationally simple. Our proposed approach is rooted in modeling the geometry along edges of the object representative graph. We subsequently define a new topo-geometric skeleton that we call *squigraph*. The key idea for the geometric modeling of shapes is to embed in Euclidean space a manifold of new characteristic curves (we refer to as *iso-geodesic* curves) of an object surface. The resulting embedding space, as we show below, is $\mathbb{R}^3$, and the curve manifold is 1-D, i.e., a space curve in $\mathbb{R}^3$. As a result, all topological and geometric information we exploit remains intrinsic to the modeled object, hence preserving all desired invariance properties alluded to earlier.

The remainder of the paper is organized as follows: In Section II, we briefly overview the topological modeling phase, and

Manuscript received February 03, 2009; revised September 11, 2009. First published October 16, 2009; current version published January 15, 2010. This work was supported in part by the U.S. Air Force Office of Scientific Research under Grant FA9550-07-1-0104. The associate editor coordinating the review of this manuscript and approving it for publication was Dr. Arun Abraham Ross.

The authors are with the Electrical and Computer Engineering Department, North Carolina State University, Raleigh, NC, 27695 USA (e-mail: djamila.aouada@ieee.org; ahk@ncsu.edu).

Color versions of one or more of the figures in this paper are available online at http://ieeexplore.ieee.org.

Digital Object Identifier 10.1109/TIP.2009.2034693

define the notation used throughout this paper. In Section III, we describe our technique of embedding the geometry in $\mathbb{R}^3$ and present the resulting modeling curve. In Section IV, we explain how we construct squigraphs and use them to quantify the geometric dissimilarity between 3-D shapes. We finally substantiate the development with many examples, and discuss the attributes of our proposed model in Section V.

## II. Topological Reeb Graphs

In this work, we view 3-D objects as 2-D smooth and compact surfaces $\mathcal{S}$ embedded in $\mathbb{R}^3$. In order to extract topological features of 3-D objects, we make an extensive use of *Morse theory* [15], [16]. Morse theory states that it is possible to define a particular smooth function $f(\cdot)$ on a smooth surface $\mathcal{S}$, and track its critical points in order to study the topology of $\mathcal{S}$. Such a function $f(\cdot)$ is called Morse function and is defined as follows.

*Definition 1 (Morse Function):* A smooth function $f : \mathcal{S} \rightarrow \mathbb{R}$ on a smooth manifold $\mathcal{S}$ is called *Morse* if all of its critical points are nondegenerate.

A standard Morse function is a *height* function [5], [7], [12], [16], [18]. The image of a point $\mathbf{p}$ on $\mathcal{S}$ via the height function is reduced to its $z$ coordinate as shown in Fig. 1(b). Any representation that is based on the height function is clearly *geometrically* variant, as critical points of a surface in $\mathbb{R}^3$ will change as a result of its mere rotation. Since shape descriptors are, for a large number of applications, required to be invariant to similarity transforms[1], a choice of an appropriate Morse function is critical. In [11], Hilaga *et al.* define a Morse function for generic metrics on surface, that is invariant to isometric transforms. Specifically, this function is defined at every point $\mathbf{v}$ on $\mathcal{S}$ as the integral of the geodesic distance $\mathbf{d}(\mathbf{v},\mathbf{p})$ from $\mathbf{v}$ to all other points $\mathbf{p}$ on $\mathcal{S}$

$$f(\mathbf{v}) = \int_{\mathbf{p}\in\mathcal{S}} \mathbf{d}(\mathbf{v},\mathbf{p}) d\mathcal{S}. \tag{1}$$

A discrete approximation $g(\cdot)$ of (1) is defined in [8], and referred to as *Global Geodesic Function* (GGF), such that

$$g(\mathbf{v}) = \frac{\sum\limits_{\mathbf{p}\in\mathcal{S}} \mathbf{d}(\mathbf{v},\mathbf{p})}{\max_{\mathbf{q}\in\mathcal{S}} \left( \sum\limits_{\mathbf{p}\in\mathcal{S}} \mathbf{d}(\mathbf{q},\mathbf{p}) \right)}. \tag{2}$$

We choose the GGF to be our Morse function and show an example in Fig. 1(c), where the considered surface $\mathcal{S}$ is the double torus illustrated in Fig. 1(a). In addition to its independence of any reference point, an important property of this Morse function is its invariance to isometric transformations, thus yielding a consistent and unique characterization of an object surface. The independence of reference points is achieved by the geodesic integration procedure at each point. The normalization of the functional shown in (2) ensures an invariance to scaling by making the range of $g(\cdot)$ coincide with $[g_0, 1]$, with $g_0 = \left( \min_{\mathbf{v}\in\mathcal{S}} \sum_{\mathbf{p}\in\mathcal{S}} \mathbf{d}(\mathbf{v},\mathbf{p}) / \max_{\mathbf{v}\in\mathcal{S}} \sum_{\mathbf{p}\in\mathcal{S}} \mathbf{d}(\mathbf{v},\mathbf{p}) \right)$ and $g_0 > 0$. In Fig. 1(c), we show the color coding map for $g(\cdot)$ used on all our objects. Additional analytical and computational details on the GGF may be found in [8]. With $g(\cdot)$ in hand, we proceed to construct a topological Reeb graph for $\mathcal{S}$ [4], [11]. Mathematically, a Reeb graph is a quotient space $\mathcal{S}/\sim$, where the equivalence relation is given by $\mathbf{p} \sim \mathbf{q}$ if and only if $g(\mathbf{p}) = g(\mathbf{q})$ with $\mathbf{p}$ and $\mathbf{q}$ being two points on $\mathcal{S}$ and belonging to the same connected component of $g^{-1}(g(\mathbf{p}))$. Practically, we sample the surface $\mathcal{S}$ of a 3-D object by way of level sets of a Morse function, and in our case thereof a GGF $g(\cdot)$. As illustrated in Fig. 1(d), the level sets of $g(\cdot)$ are closed curves, which we refer to as *iso-geodesic* curves. We present the resulting Reeb graph in Fig. 1(e), where each closed iso-geodesic curve is replaced by a node colored in black.

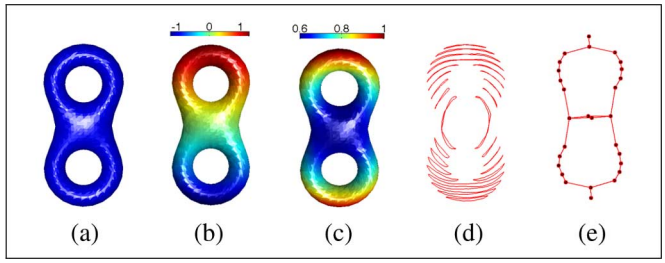


Fig. 1. Illustration of Reeb graph extraction. (a) Initial object. (b) Height function on the surface. (c) GGF function on the surface. (d) Iso-geodesic curves. (e) Extracted topological Reeb graph. (Best visualized in color).

## III. Representation of a Surface Geometry

We note that, just as in [4] and [5], our 3-D object modeling approach starts with a topological analysis followed by a geometrical analysis step. In our present work, however, we strive to achieve a topo-geometric representation that is both discriminative and efficient. This is why we proceed by economically exploiting, for the geometric modeling, the same entities used earlier for the topological modeling with Reeb graphs. The entities in question are the level sets of the GGF, i.e., the iso-geodesic sets defined on the surface of an object. Using iso-geodesic sets allows us to further extend the invariance properties of the GGF to the geometric phase.

In addition, unlike the usual global shape descriptors, a more complete geometric representation is one which provides a local description taking into account the spatial location of points or vertices [3]. The iso-geodesic curves used in the topological representation consequently appear, once again, to be able to offer perfect local geometric descriptors. We, therefore, take advantage of these already extracted entities, and use them for the second phase of our modeling as described in what follows.

We note that in this paper, we skip over the topological modeling that we illustrate in Fig. 2(b) and develop in [9], and focus on geometric characterization. We will, in addition, use the geometry of an object as the basis for object comparison/matching applications. Broadly, our strategy is as follows: once we extract iso-levels of the GGF, we obtain a set of closed curves (namely the iso-geodesic curves) along each edge of a topological graph of an object. We use these characteristic curves to define a geometric model. We subsequently assign the models to the corresponding edges. We in turn exploit these geometric models to further compare every two edges that have been matched as

[1]Similarity transforms include: translation, rotation, and scaling, or any combination thereof.

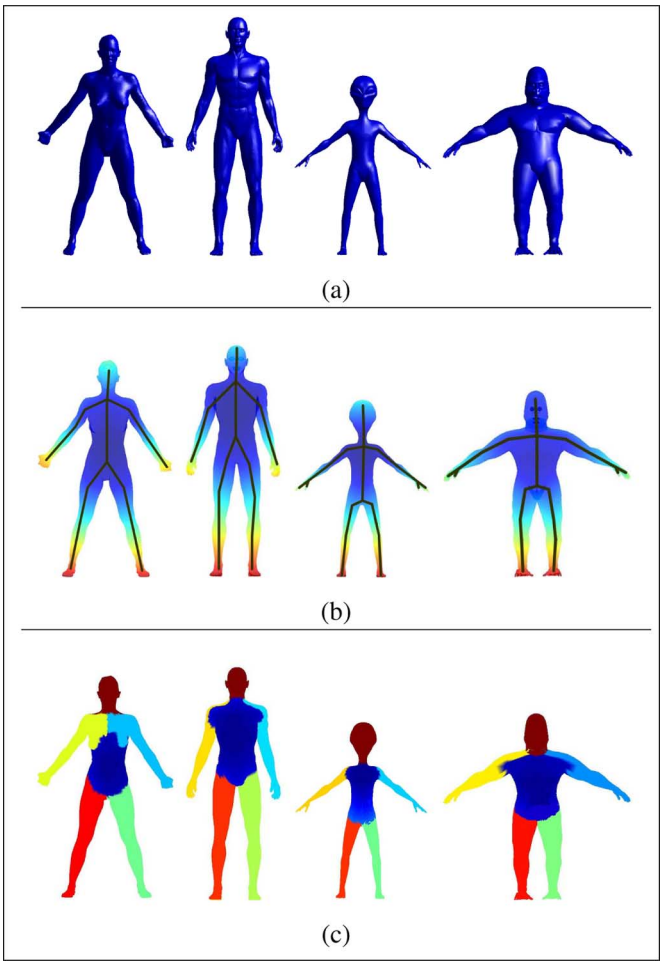


Fig. 2. Overview of the targeted problem (Best visualized in color): the four 3-D models (Princeton data set [31]) in (a) are from the same class because they are topologically similar as shown in (b). There is still a difference to be detected at the geometrical level. In (c), the part by part comparison is illustrated. We measure the dissimilarity between homogeneous parts that have been topologically matched. They are represented by edges in (b), and by the same color in (c).

part of two topologically similar graphs. In Fig. 2(c), we show all matched edges in the same color.

We compactly represent the final topo-geometric model through a new spatial graph that we call *squigraph* (Fig. 6(d)). A squigraph graph differs from a classical Reeb graph by its "squiggling" curves that replace the standard straight edges and encode the geometric information about the shapes.

### A. Level Set Characterization of a Surface

Generically, we can reconstruct a 2-D surface $\mathcal{S}$ from the set of 1-D iso-levels of the GGF. A surface $\mathcal{S}$ is then a disjoint union of all iso-geodesic sets $\mathcal{A}(t)$ for $t \in [g_0, 1] \subset \mathbb{R}^+$, where $\mathcal{A}(t) = \{\mathbf{v} \in \mathcal{S} \,|\, g(\mathbf{v}) = t\}$, and $g_0$ is the minimal value of $g(\cdot)$

$$\mathcal{S} = \bigcup_{t=g_0}^{t=1} \mathcal{A}(t), \text{ and } \mathcal{A}(t_1) \cap \mathcal{A}(t_2) = \varnothing \text{ if } t_1 \neq t_2. \quad (3)$$

For smooth and compact objects, an iso-geodesic set is the union of closed curves (i.e., iso-geodesic curves). The number of these distinct curves at the same geodesic level is the cardinality $Car(t)$ of the corresponding iso-geodesic set $\mathcal{A}(t)$.

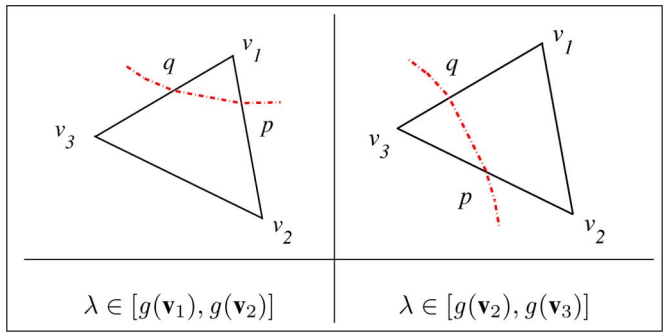


Fig. 3. Covering face and iso-geodesic curve interpolation.

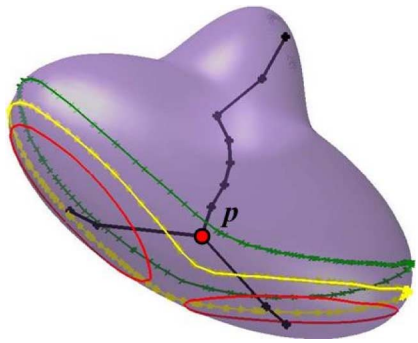


Fig. 4. Illustration of topological change of iso-geodesic curves. The point $p$ is the bifurcation point at which this change occurs.

In practice and on triangulated meshes, the extraction of an iso-geodesic set for a given level, say $\lambda$, entails first finding all the faces that cover this set of curves. Each iso-geodesic curve is included in a connected set of covering faces so that the resulting curve is ensured to be closed. A covering face whose vertices are $\mathbf{v}_1$, $\mathbf{v}_2$, and $\mathbf{v}_3$, with $g(\mathbf{v}_1) < g(\mathbf{v}_2) < g(\mathbf{v}_3)$, falls under one of the following properties:

1) $\lambda \in [g(\mathbf{v}_1), g(\mathbf{v}_2)]$ or
2) $\lambda \in [g(\mathbf{v}_2), g(\mathbf{v}_3)]$

Two points $\mathbf{p}$ and $\mathbf{q}$ belonging to the approximated iso-geodesic set $\mathcal{A}(\lambda)$ are defined on two edges of the covering face (Fig. 3). If Property 1 is verified, then

$$\overrightarrow{\mathbf{v}_1\mathbf{p}} = \frac{\lambda - g(\mathbf{v}_1)}{g(\mathbf{v}_2) - g(\mathbf{v}_1)} \cdot \overrightarrow{\mathbf{v}_1\mathbf{v}_2}$$

and

$$\overrightarrow{\mathbf{v}_1\mathbf{q}} = \frac{\lambda - g(\mathbf{v}_1)}{g(\mathbf{v}_3) - g(\mathbf{v}_1)} \cdot \overrightarrow{\mathbf{v}_1\mathbf{v}_3}.$$

If instead Property 2 is verified, then

$$\overrightarrow{\mathbf{v}_3\mathbf{p}} = \frac{g(\mathbf{v}_3) - \lambda}{g(\mathbf{v}_3) - g(\mathbf{v}_2)} \cdot \overrightarrow{\mathbf{v}_3\mathbf{v}_2}$$

and

$$\overrightarrow{\mathbf{v}_3\mathbf{q}} = \frac{g(\mathbf{v}_3) - \lambda}{g(\mathbf{v}_3) - g(\mathbf{v}_1)} \cdot \overrightarrow{\mathbf{v}_3\mathbf{v}_1}.$$

Once we obtain all the possible couples $(\mathbf{p}, \mathbf{q})$, we smoothly interpolate, with a B-spline for instance, the so obtained sample of points to get the iso-geodesic curve at the level $\lambda$ of the GGF; moreover, the subsurface supported by one edge has exactly one iso-geodesic curve for every value between $a$ and $b$; the extremal

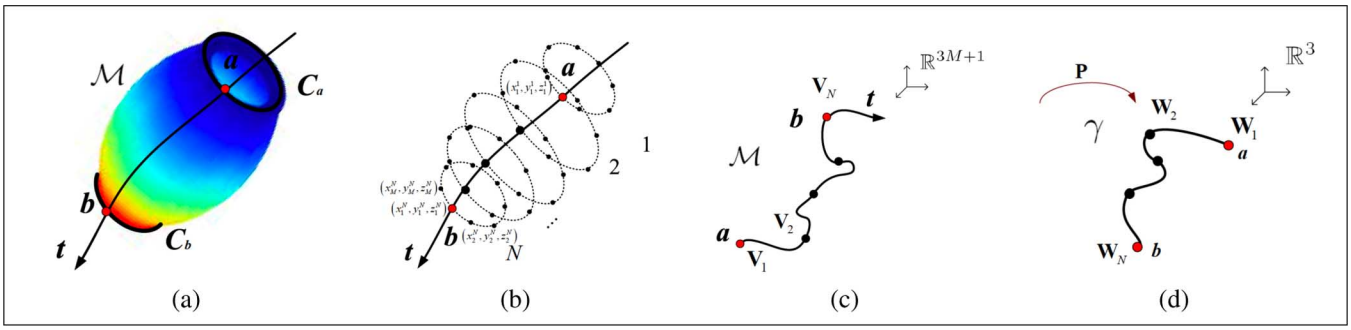


Fig. 5. Geometric modeling of a mono-cardinality subsurface $\mathcal{M}$: (a) the GGF on $\mathcal{M}$ is strictly monotonous and takes its values in the interval $[a, b]$. As a result, the two bounding iso-geodesic curves are $C(a)$ and $C(b)$. (b) Discretized version of $\mathcal{M}$. (c) Path created by $\mathcal{M}$ in high-dimensional space. (d) Final modeling curve in 3-D space.

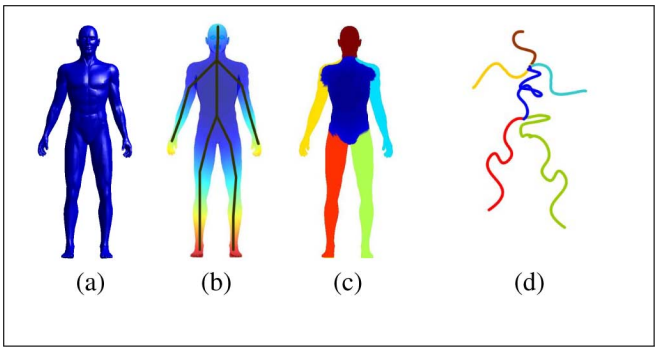


Fig. 6. Object representation using a *squigraph*. (a) Original shape. (b) Extracted Reeb graph. (c) Partitioning into primitives. (d) Squigraph for a topo-geometric representation.

values of the GGF along the edge. We call such subsurface $\mathcal{M}$ a *mono-cardinality* subsurface. We may view $\mathcal{M}$ as follows:

$$\mathcal{M} = \bigcup_{t\in[a,b]} C(t)$$
$$\text{with } g_0 \le a < b \le 1$$
$$\text{and } C(t_1) \cap C(t_2) = \varnothing \text{ if } t_1 \neq t_2 \tag{4}$$

where $C(t)$ is just one iso-geodesic curve at the level $t$ of the GGF. In the example of Fig. 4, the illustrated iso-geodesic sets correspond (from top to bottom) to the values 0.8, 0.85 and 0.9 of the GGF, respectively. The corresponding cardinalities are $Car(0.80) = Car(0.85) = 1$, and $Car(0.90) = 2$, i.e., the first two sets consist of one closed curve, whereas the third set includes two distinct closed curves. Tracking the cardinalities of iso-geodesic sets helps us in constructing an associated Reeb graph. The continuous and smooth evolution of the iso-geodesic curves on a surface captures its topological and geometrical description. Any change in the topology of the iso-geodesic sets, i.e., any smooth change in their cardinalities, hence, determines a bifurcation point as shown in Fig. 4. This transition is translated on the object's topological graph by a node of order $\eta > 2$ that introduces $\eta$ edges. We preserve all such nodes and those corresponding to critical points of the GGF along with their edges to only capture the important topological information. The resulting special skeleton, that we refer to as a *reduced 3-D Reeb graph*, offers a nice structure on which the geometry of an object may easily be superposed. Thus, the geometric modeling of a complex shape is now reduced to separately modeling a partial shape along each edge of the reduced Reeb graph. We next discuss the details of modeling the geometric shape along an edge.

### B. Whitney Theorem for Modeling

It is important to note that a geometric shape along an edge corresponds to what we described, in Section III-A, as a mono-cardinality subsurface. So all the partial shapes along Reeb graph edges are simply equivalent to generalized cylinders. In fact, this philosophy of decomposing a complex shape into a set of cylinders goes back to the very early work on shape recognition by components [24].

Equation (4) shows that a mono-cardinality subsurface $\mathcal{M}$ is formed by the disjoint union of an infinite number of *iso-geodesic* curves $C(t)$, monotonically and continuously parameterized by $t \in [a, b] \subset \mathbb{R}^+$, where $[a, b]$ is the range of the GGF restricted to $\mathcal{M}$ [Fig. 5(a)]. It, therefore, naturally follows that $\mathcal{M}$ is a smooth path in high-dimensional space whose point elements are the iso-geodesic curves $C(t)$, $t \in [a, b]$; hence, $\mathcal{M}$ constitutes a smooth 1-D manifold on the topological space of closed iso-geodesic curves on which the restriction of the GGF is a homeomorphism [Fig. 5(c)]. In what follows, we interchangeably use $\mathcal{M}$ to refer to the mono-cardinality subsurface embedded in $\mathbb{R}^3$, as well as to the corresponding curve embedded in the higher dimensional space.

Getting back to our objective of simply modeling each mono-cardinality subsurface $\mathcal{M}$, we first invoke the *Whitney embedding* theorem as stated below,

*Theorem 1 (Whitney Embedding Theorem):* [17] Let $\gamma$ be an n-dimensional compact Hausdorff $C^r$ manifold, $2 \le r \le \infty$. Then, there is a $C^r$ embedding of $\gamma$ in $\mathbb{R}^{2n+1}$.

In the present problem, the manifold $\gamma$ is nothing but $\mathcal{M}$, for which the dimension $n$ is equal to one; hence, the stated theorem asserts the existence of an embedding of $\mathcal{M}$ in $\mathbb{R}^3$. In fact, such embeddings have full measure in the set of maps or even projections into $\mathbb{R}^3$, so we can assume that a random projection works. Thus, we can safely use this embedding for our geometric modeling since, by definition, an embedding preserves the geometry and does not introduce any new intersections in the new space. In practice, we approximate $\mathcal{M}$ with a finite number $N$ of iso-geodesic curves as illustrated in Fig. 5 (b). On

each curve, we take $M$ uniformly spaced points $\mathbf{v}_j^i$ defined by their Euclidean coordinates $\left(x_j^i, y_j^i, z_j^i\right)$, $i = 1, 2, \ldots, N$, and $j = 1, 2, \ldots, M$. Each curve is now a point in $\mathbb{R}^{3M+1}$ represented by the column vector $\mathbf{V}_i$, $i = 1, 2, \ldots, N$ [Fig. 5(c)], such that

$$\mathbf{V}_i = \left[\left[\mathbf{V}_1^i\right]^T \ldots \left[\mathbf{V}_M^i\right]^T\right]^T \text{ with } \mathbf{V}_j^i = \left[x_j^i, y_j^i, z_j^i\right]^T. \quad (5)$$

The sample set of iso-geodesic curves on $\mathcal{M}$ is a matrix $\mathbf{V}$ of dimension $3M \times N$ where $\mathbf{V} = [\mathbf{V}_1 \cdots \mathbf{V}_N]$. Applying the Whitney theorem on $\mathbf{V}$ reduces the embedding problem to a simple linear formulation

$$\mathbf{W} = \mathbf{P}^T\mathbf{V} \quad (6)$$

where $\mathbf{W}$ is a set of $N$ points in $\mathbb{R}^3$ resulting from the projection of $\mathbf{V}$ via $\mathbf{P}$ into $\mathbb{R}^3$. In other words, as illustrated in Fig. 5(d), the manifold $\mathcal{M}$ is reduced to a space curve $\gamma$ whose sample points are represented by the columns of the matrix $\mathbf{W}$. In Fig. 6, we illustrate the idea of a topo-geometric modeling via the space modeling curves that we just defined; hence, we intrinsically enhance the typical 3-D Reeb graph of Fig. 6(b). To that end, we assign one modeling curve to each edge of the Reeb graph. By so doing, we may view the final representation as a new kind of graph, that we refer to as a *squigraph*, as shown in Fig. 6(d). The Whitney embedding theorem guarantees that almost any projection of $\mathcal{M}$ is an embedding. In [19] and [20], the notion of *good Whitney embedding* is introduced to identify a class of projections. For many applications, such as recognition, a unique representation of an object is required. As a result, we apply the notion of *optimal embedding* with the performance criterion presented in [20] and defined in (8) being maximized.

We recall that an embedding gives us a one-to-one mapping between the path in high-dimensional space $\mathcal{M} \subset \mathbb{R}^{3M}$, and the path $\gamma \subset \mathbb{R}^3$, so that no two points in $\mathcal{M}$ will collapse as a result of the mapping in (6). An implementation of this principle is presented in [20] and referred to as a *secant based method*. As just explained, no two points in $\mathbb{R}^{3M}$ are mapped to the same point in $\mathbb{R}^3$. This means that the projecting vector is linearly independent from any possible secant[2] in $\mathbb{R}^{3M}$. We define the set of all possible unit secant vectors from the initial data $\mathbf{V}$ as follows:

$$\begin{aligned}\mathbf{\Psi} &= \left\{\frac{\mathbf{V}_i - \mathbf{V}_j}{\|\mathbf{V}_i - \mathbf{V}_j\|}, (i,j) \in \{1, \ldots, N\}^2 \text{ and } i \neq j\right\} \\ &= \{\mathbf{\Psi}_i, i = 1, \ldots, L\}\end{aligned} \quad (7)$$

with $L = (N!/(N-2)!2!)$.

The performance of the projection operator $\mathbf{P}$ is then reflected by

$$\epsilon = \min_{i=1,\ldots,L} \left[\left\|\mathbf{P}^T\mathbf{\Psi}_i\right\|_2\right]. \quad (8)$$

The closer $\epsilon$ is to 1, the better spread out the projected points in $\mathbb{R}^3$ are, and the better the choice of $\mathbf{P}$ is; hence, finding a good estimate of the optimal projection is reduced to the following minimization problem:

[2]*Secant* or *secant line* is a line that intersects two points from a curve.

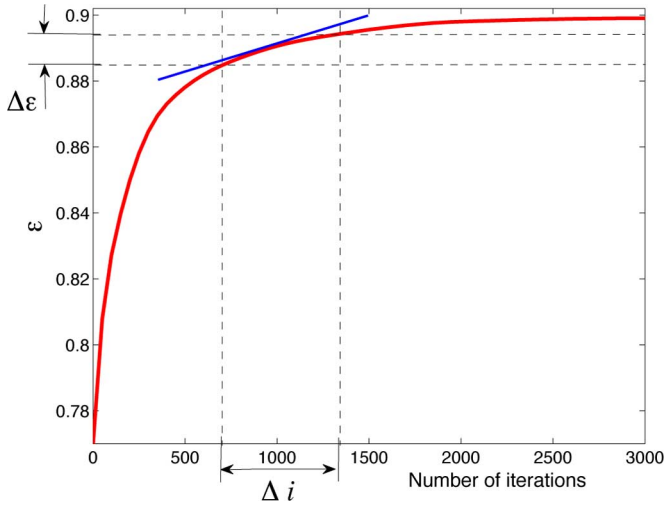


Fig. 7. Asymptotic convergence of LTMADS applied to 3-D shape data set.

$$\begin{aligned}\hat{\mathbf{P}} &= \arg\min\left[-\min_{i=1,\ldots,L}\|\mathbf{P}\mathbf{\Psi}_i\|_2\right] \\ &= \arg\min F(\mathbf{P}).\end{aligned} \quad (9)$$

Since the function $F(\mathbf{P})$ is non differentiable, we need a direct search algorithm that does not require any derivative of the function to minimize it. As presented in [21], the *Lower Triangular Mesh Adapted Direct Search algorithm* (LTMADS) has been adapted to Riemannian manifolds and tested on an example of a Whitney embedding. The solution given by LTMADS is highly dependent on the initial data. On our 3-D objects, the performance of LTMADS converges asymptotically to 1 (Fig. 7). We define a stopping criterion for the LTMADS algorithm adapted to each data by considering the slope $\Delta\epsilon = |\epsilon_i - \epsilon_{i-1}|$, where $\epsilon_i$ and $\epsilon_{i-1}$ respectively represent the performances of the optimization algorithm at iterations $i$ and $i-1$.

### C. Space Marking

It is important to ensure that all iso-geodesic curves' discrete representations are uniform and consistent within a coordinate space. Visually, we may equate this task to marking the surface $\mathcal{M}$. By marking, we mean drawing a well defined reference line on the surface $\mathcal{M}$. In Fig. 5(a), this reference line is the one curve going through the two red points corresponding to levels $a$ and $b$. This special line enables us to construct the vectors $\mathbf{V}_i$ in an accurate and consistent manner. To that end, in addition to the iso-geodesic curves, we introduce a new characteristic curve that we refer to as an *orthogonal curve*, and define as follows:

*Definition 2 (Orthogonal Curves):* An orthogonal curve on a surface $\mathcal{S}$ passing through a point $\mathbf{p}$ is the curve of minimal length linking the iso-geodesic curve containing $\mathbf{p}$ to another iso-geodesic curve.

We note that the vector field generated by the gradient of the GGF gives integral curves orthogonal to the iso-geodesic curves. So by definition, an orthogonal curve takes a point $\mathbf{p}$ on a surface $\mathcal{S}$ and geodesically projects it on another iso-geodesic curve (Fig. 8). By considering an infinitesimal patch around a point $\mathbf{p}$ from $\mathcal{S}$, we approximate the patch by a disk on which

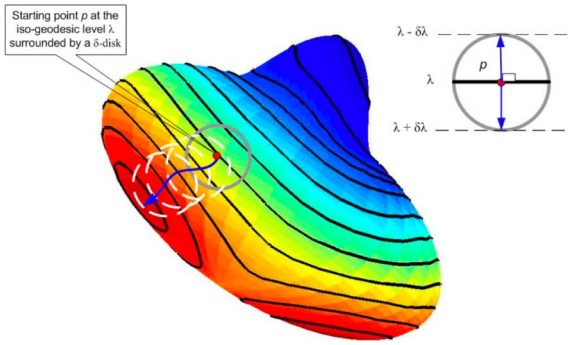


Fig. 8. Orthogonal curve extraction using infinitesimal patches around each point at increasing values of the GGF.

the iso-geodesic curve $C$ becomes a segment passing through $\mathbf{p}$. This segment represents the direction of zero variation of the GGF. We find that the projection of $\mathbf{p}$ on the next iso-geodesic segment $C'$ follows the perpendicular to $C$ on $\mathbf{p}$. Under the assumption that all points are uniformly distributed on the surface and since the iso-geodesic curve represents the direction of zero variation of the GGF, we conclude, by duality, that the orthogonal projection of $\mathbf{p}$ is equivalent to finding the direction $e$ of highest variation of the GGF; hence, we construct an orthogonal curve by progressively tracking, at a point level, the direction of the highest variation of the GGF. We determine the direction $e$ that maximizes the directional derivative of $g$ at a point $\mathbf{p}$; thus, we extract an orthogonal curve by progressively estimating a new direction $\hat{e}$ starting at each new iso-geodesic level. We may write:

$$\begin{aligned}\hat{e} &= \arg\max\left(Dg \cdot e(\mathbf{p})\right) \\ &= \arg\max\left(\lim_{t\to 0}\frac{g(\mathbf{p}+te)-g(\mathbf{p})}{t}\right). \end{aligned} \tag{10}$$

We note that we only need a starting point to extract an orthogonal curve. This point, however, is not unique as it is only required to be a point from a bounding iso-geodesic curve ($C(a)$ or $C(b)$ in Fig. 5). In fact, thanks to the construction proposed in (5), choosing a different starting point will only result in a mere rotation of the reference axes in $\mathbb{R}^{3M}$. Besides, because in the present geometric modeling we require a full invariance to Euclidean transforms, this rotation will have no effect on the final modeling curve [$\gamma$ in Fig. 5(d)]. Starting from a point with the lowest value of the GGF, and by progressively finding $\hat{e}$, we construct an *orthogonal curve* with respect to iso-geodesic curves. By construction, iso-geodesic curves are transversal to an orthogonal curve. Consequently, a subset of the surface $\mathcal{M}$ can be modeled by a fiber bundle whose base curve is an orthogonal curve and whose bundles are the associated iso-geodesic curves as illustrated in Fig. 5(b).

## IV. Three-Dimensional Shape Comparison

Our proposed squigraph model provides a topological and a geometric representation. The topological representation is coarse, and, hence, initiates a shape comparison procedure. We call upon the additional geometric enhancement once there is a minimally significant similarity score that is attained when comparing topological Reeb graphs. In what follows, we define the necessary and applied measures at the different comparison levels.

### A. Comparison of Reeb Graphs[3]

Reeb graphs being topological descriptors, we require a connectivity information to define a distance between them. We actually use reduced Reeb graphs where the node order is never 2. We herein define a distance measure that is in the same spirit as the edit-distance for shape matching as defined in [23]. We compute in (11) the similarity score $\mathbb{S}(\cdot,\cdot)$ between two reduced Reeb graphs $\Gamma_1$ and $\Gamma_2$ with $N_1$ and $N_2$ nodes, respectively, and $N_1 \leqslant N_2$. We denote by $\{\mathbf{v}_i\}_{i=1}^{N_1}$ the nodes of $\Gamma_1$, and $\{\mathbf{w}_i\}_{i=1}^{N_2}$ the nodes of $\Gamma_2$. We define the similarity between these two graphs as follows:

$$\mathbb{S}(\Gamma_1,\Gamma_2) = \frac{2\pi\sigma}{N_1}\sum_{i=1}^{N_1}\max_{j=1,\ldots,N_2}\left\{\beta\left(\mathbf{v}_i,\mathbf{w}_j\right)\delta_i^{(\Gamma_1)}(\mathbf{w}_j)\right\} \tag{11}$$

with

$$\delta_i^{(\Gamma_1)}(\mathbf{w}_j) = \begin{cases} 1, & \text{iff } |\eta_{\mathbf{v}_i} - \eta_{\mathbf{w}_j}| \leqslant 2 \\ 0, & \text{otherwise} \end{cases}$$

and

$$\beta(\mathbf{v}_i,\mathbf{w}_j) = \frac{1}{2\pi\sigma}\exp\left(-\frac{|g(\mathbf{v}_i)-g(\mathbf{w}_j)|}{2\sigma^2}\right) \tag{12}$$

where $\sigma$ is a strictly positive constant of our choosing and $\eta_{\mathbf{v}_i}$ and $\eta_{\mathbf{w}_j}$ are the orders of nodes $\mathbf{v}_i$ and $\mathbf{w}_j$, respectively. The function $\delta_i^{(\Gamma_k)}(\cdot)$ plays the role of a registration operator based on the order of graph nodes. We also choose a kernel function $\beta(\cdot,\cdot)$ that is strictly decreasing; hence, the choice of the Gaussian kernel in (12). The intuition behind choosing the factor $\beta$ is the assignment of a high similarity weight to registered nodes if they correspond to GGF levels that are close. The choice of $\sigma$ can greatly affect the graph matching process. Indeed, it defines a margin for a good match, after which the similarity score is supposed to decay. Too large values of $\sigma$ incur no selectivity, and the matching becomes inaccurate. Too small values make the comparison rigid, and only allow high similarity scores between perfectly overlapping shapes which defeats the purpose of a multilevel comparison (coarse and fine). For our experiments, the empirical value of 0.2 provided good results. In general, and for data sets with no prior knowledge, a leaning strategy can help find a good choice for $\sigma$.

### B. Comparison of Squigraphs

In Section III, we proposed to represent the geometry of smooth 2-D mono-cardinality surfaces captured by characteristic curves by just one curve in $\mathbb{R}^3$, namely, the modeling curve. The problem of comparing 3-D objects may hence be reduced to measuring the dissimilarity between space curves up to a similarity transform. The measure we choose appears to be critical in assessing the effectiveness of the modeling curves in accurately reflecting the geometric properties of 3-D shapes. To ensure a good performance, we define a new technique for space curve comparison. The key objective of this technique is to select geometric features that are appropriate

[3]Section IV-A appeared in [22].

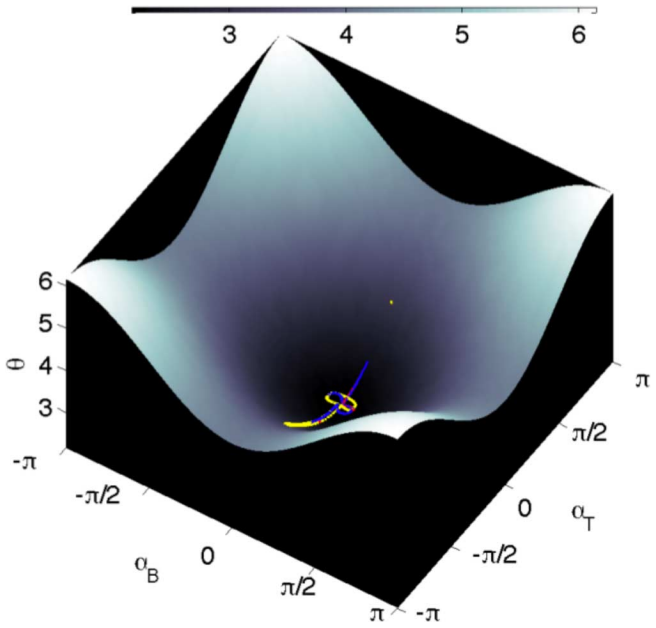


Fig. 9. Manifold defined by the invariant signature curve as defined in (11).

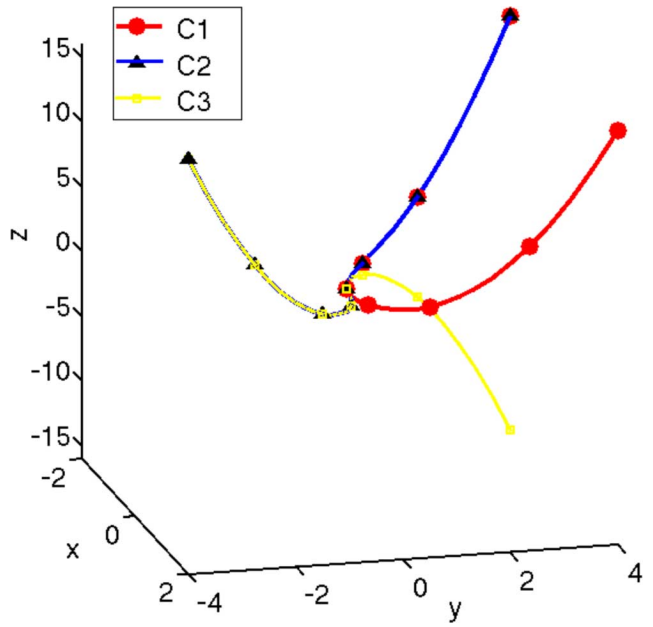


Fig. 10. $C1, C2$, and $C3$ are three similar space curves except at one inflection point.

for the present application; furthermore, we aim at defining a Riemannian metric directly on the space of these same features. By so doing, we ensure that at all stages of this work, we faithfully capture features that are fully intrinsic to the geometry of a given shape; thus, we present a new similarity invariant signature for space curves. This signature is based on the information contained in the turning angles of both the tangent and the binormal vectors at each point on the curve.

A space curve is uniquely determined, up to a Euclidean transform, by its curvature function $\kappa(t)$, and torsion function $\tau(t)$, both continuous functions of the parameter $t$ that we choose to be the arc length; hence, we naturally use these measurements to define an adequate invariant signature curve; however, since we target the group of similarity transforms, and knowing that curvature and torsion are not scale invariant, we use turning angles as the geometric features describing space curves [35]. If $\mathbf{T}$, $\mathbf{N}$, and $\mathbf{B}$ are the tangent, the normal, and the binormal vectors, respectively, we may define two turning angles $\alpha_T$ and $\alpha_B$. $\alpha_T$ is the change in the direction of $\mathbf{T}$, and $\alpha_B$ is the change in the direction of $\mathbf{B}$ such that:

$$\alpha_T(t) \approx \kappa(t) \cdot \Delta t \text{ and } \alpha_B(t) \approx \tau(t) \cdot \Delta t. \tag{13}$$

We extract the information contained in the proposed turning angles by using a notion in information theory commonly referred to as "Shannon surprisal" [35], [36]. We assume that $\alpha_T$ and $\alpha_B$ follow a *von Mises* distribution $f_\alpha(\cdot)$ with a zero mean and a spread parameter $b$ equal to 1. We extract the information contained jointly in $\alpha_T$ and $\alpha_B$ by introducing the following independent invariant signature for space curves:

$$\begin{aligned}\theta(t) &= -\ln\left(f_\alpha(\alpha_T, \alpha_B)\right) \\ &= -2\ln(A) - \cos(\alpha_T(t)) - \cos(\alpha_B(t))\end{aligned} \tag{14}$$

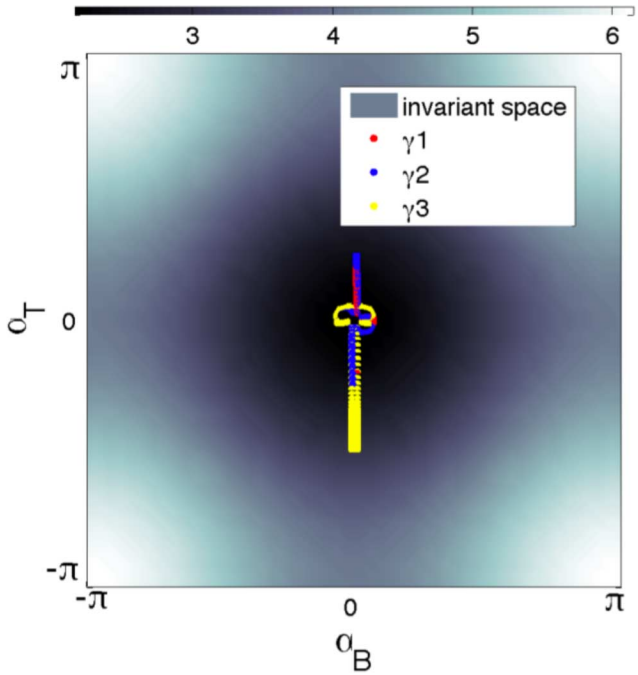


Fig. 11. Invariant signature curves for 3-D modeling curves $\gamma 1$, $\gamma 2$, and $\gamma 3$; the same curves appearing in Fig. 9.

with $(\alpha_T(t), \alpha_B(t)) \in ([-\pi, \pi])^2$ and $A = (1/2\pi \cdot \text{Bessel}(0, b))$. $\text{Bessel}(0, b)$ being the Bessel distribution of mean 0 and variance $b$. The range of the new function $\theta(\cdot)$ constitutes a curved space $\mathcal{T}$, as shown in Fig. 9. For instance, for the three space curves $C1$, $C2$, and $C3$ in Fig. 10, the corresponding invariants are represented in Fig. 9. For clarity, we show the projections of these same invariant curves in Fig. 11. We note the discrimination power of these invariants, as they show the ability to distinguish between curves that differ by one inflection point.

All the invariant signatures are thus constrained to live on the defined invariant space. We view an invariant signature curve as the trace for the corresponding geometry. Defining $\mathcal{T}$ as the space of possible traces is a natural way to register them. As a consequence, we may directly apply a distance measure to compare these traces with no need for worrying about prior registration of the traces. We thus choose to compare two traces $\gamma 1$ and $\gamma 2$, corresponding to two modeling curves $C1$ and $C2$, by considering the oriented curve $\gamma_\Delta = \gamma 1 - \gamma 2$. We use tools from measure theory and choose to refer to their physical intuition in relating them to our problem [25], [26]. We start by viewing the oriented version of the space $\mathcal{T}$ as a vector field $\overrightarrow{\mathbf{F}}$ on the $(2\pi \times 2\pi)$ plane defined by the variables $\alpha_T$ and $\alpha_B$. We directly relate $\overrightarrow{\mathbf{F}}$ to $\theta(t)$, and define it as follows:

$$\begin{aligned}\overrightarrow{\mathbf{F}} &: ([-\pi,\pi])^2 \to \mathbb{R}^2 \\ &(\alpha_T,\alpha_B) \mapsto -\ln\left(f_\alpha(\alpha_T)\right)\overrightarrow{i} - \ln\left(f_\alpha(\alpha_B)\right)\overrightarrow{j}.\end{aligned}$$

This may also be written as

$$\begin{aligned}\overrightarrow{\mathbf{F}}(t) &\equiv \overrightarrow{\mathbf{F}}(\alpha_T,\alpha_B), \\ &= -\begin{pmatrix}\ln(A)+\cos(\alpha_T(t)) \\ \ln(A)+\cos(\alpha_B(t))\end{pmatrix}. \end{aligned} \tag{15}$$

We define $\gamma_\Delta^*$; the projection of $\gamma_\Delta$ on the $(2\pi)^2$ plane. $\gamma_\Delta^*$ is a 1-current in the space dual to the space of 1-forms $\mathcal{D}^1([-\pi,\pi])^2$. This means that $\forall\, \phi \in \mathcal{D}^1([-\pi,\pi])^2$

$$\begin{aligned}\gamma_\Delta^*(\phi) &:= \int_{\gamma_\Delta^*} \phi \\ &= \int_{\gamma_\Delta^*} \phi(\overrightarrow{\mathbf{F}}(t))\, dt. \end{aligned} \tag{16}$$

With these notions in hand, we naturally use the flat norm $\mathbb{F}(\gamma_\Delta^*)$ as the intrinsic distance between two mono-cardinality surfaces $\mathcal{S}1$ and $\mathcal{S}2$ whose modeling curves are $C1$ and $C2$, and whose traces are $\gamma 1$ and $\gamma 2$, respectively. We thus may write

$$\begin{aligned}&\mathbb{D}(\mathcal{S}1,\mathcal{S}2) \\ &\quad = \mathbb{F}(\gamma^*1 - \gamma^*2), \\ &\quad := \sup\{\gamma_\Delta^*(\phi) : ||d\phi|| \leqslant 1 \text{ for all } ||\phi|| \leqslant 1\}\end{aligned} \tag{17}$$

where $\gamma_\Delta^* = (\gamma^*1 - \gamma^*2)$. The advantages of defining this comparison technique are clearly presented in a different paper. We furthermore define a global metric for the comparison of complex squigraphs. So we consider that $\mathcal{S}1$ and $\mathcal{S}2$ are now two compound 2-D surfaces such that each one is composed of $N$ mono-cardinality surfaces $\mathcal{S}1^i$ and $\mathcal{S}2^i$, $i = 1,\ldots,N$

$$\mathcal{S}1 = \bigcup_{i=1}^{N} \mathcal{S}1^i, \text{ and } \mathcal{S}2 = \bigcup_{i=1}^{N} \mathcal{S}2^i. \tag{18}$$

We define the new distance between the two surfaces $\mathcal{S}1$ and $\mathcal{S}2$ as follows:

$$\begin{aligned}\mathbb{D}(\mathcal{S}1,\mathcal{S}2) = \frac{1}{2}\sum_{i=1}^{N}&\left(\frac{\text{area}\left(\mathcal{S}1^i\right)}{\text{area}\left(\mathcal{S}1\right)} + \frac{\text{area}\left(\mathcal{S}2^i\right)}{\text{area}\left(\mathcal{S}2\right)}\right) \\ &\cdot\mathbb{D}\left(\mathcal{S}1^i,\mathcal{S}2^i\right).\end{aligned} \tag{19}$$

We run the topological matching of objects with the distance $\mathbb{S}$ defined in (11) prior to running the geometrical comparison with the distance $\mathbb{D}$. In our experiments we use both distances but will only analyze the geometric comparison as it is the focus of this paper.

## V. Experiments

We experimentally investigate the performance of the proposed shape modeling technique. Throughout our definition and presentation of squigraphs, we have shown how rich they are in information. In what follows, we illustrate how to exploit this information for different levels of discrimination and for different application objectives; furthermore, we investigate the robustness properties of squigraphs through some pertinent examples.

### A. Discrimination Power

To assess the overall discrimination power of squigraphs, we compare their performance to those of well established approaches. Our comparison involves the following techniques.

- Probability density function (PDF) descriptors: Using the distributions of surface features is a technique that was first clearly defined and analyzed by Funkhouser *et al.* [30]. In our experiments, we use the GGF as the surface feature, and its distribution as the shape descriptor. We choose the *Jensen-Shannon* Divergence (JSD) as the dissimilarity measure between the GGF distributions [12], [28]–[30].
- Classification by Characteristic Resolution (CCR) [8]: We have shown in [8] that each class of shapes determines a characteristic resolution.[4] This parameter is extracted through a global comparison of the distribution of the GGF for each class of 3-D objects. In short, we may define the characteristic resolution as being the lowest resolution at which all class members will be accurately represented.
- Augmented Multiresolution Reeb Graph (aMRG) [4]: This technique is the closest to squigraphs because of its two-level philosophy, and because of the similar Morse function it primarily uses in defining a Reeb graph. aMRG is a technique that has been experimentally established to outperform many 3-D classification techniques including the method of spherical harmonics [37].

To be able to compare all these different techniques on the same basis we use Receiver Operating Characteristic curves (ROC) as illustrated in Fig. 12. We then use the Area Under the Curve (AUC) as our measure for classification performance. We use the Princeton [31] and the Technion data sets [32]–[34] for a total of 17 classes and 239 objects. The overall performance AUC for each technique is summarized in Table I. With a little more than 97% of overall performance, we note that *squigraphs* outperform other techniques. Doing better than PDF and CCR is quite expected as these two techniques only provide a global description of a complex shape. It becomes more challenging to clearly distinguish between two objects whose global shapes are very similar. As presented earlier in Section I, aMRG and *squigraphs* are multilevel descriptors which enable them to capture global, as well as local features. We explain the better performance of *squigraphs* over aMRG by the nature of the

[4]Resolution: is the number of vertices used to describe a given shape.

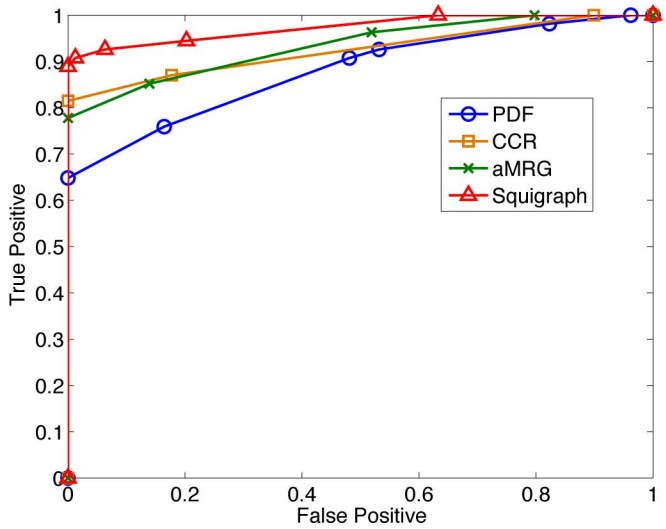


Fig. 12. ROC curves comparing different classification techniques.

TABLE I
OVERALL PERFORMANCE SUMMARY

| Method | PDF | CCR | aMRG | Squigraph |
|---|---|---|---|---|
| AUC | 87.95% | 92.53% | 93.389% | 97.35% |

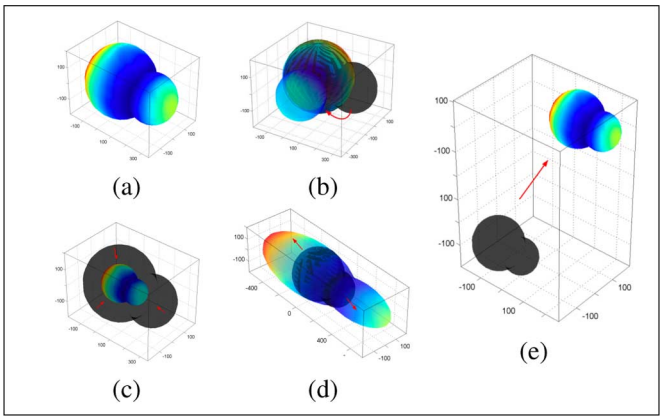


Fig. 13. Invariance to pose. The original object represented in (a) is subjected to: (b) a rotation transform, (c) a scaling transform, (d) a shearing transform and in (e) to a translation. (Best visualized in color).

features extracted locally. Indeed, while both methods extract coarse topological graphs from fully intrinsic representations, i.e., a geodesic distance independent of any reference point, aMRG relies on local features that relate to a Euclidean-based distance. So, the key advantage of the *squigraph* representation technique, that played in the results of Fig. 12, is to consistently use intrinsic features and geodesic distances.

## B. Primitive Shape Analysis

In order to thoroughly understand *squigraphs* and their modeling abilities, we propose, in the following set of experiments, to investigate the different properties a 3-D descriptor is required to enjoy. Since the proposed technique proceeds to separately consider homogeneous parts constituting an object, i.e., monocardinality subsurfaces, it is intuitively easier to start visualizing the different properties of objects with *primitive geometries*. By

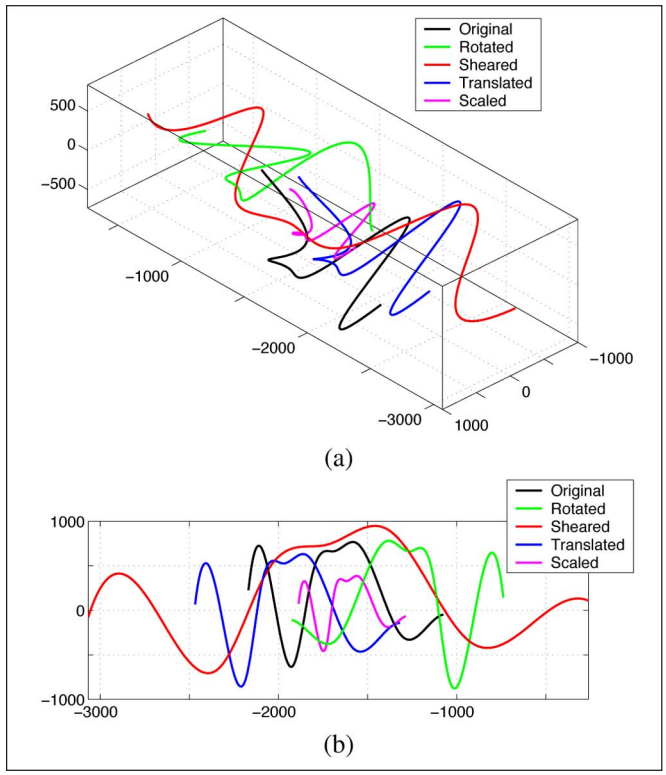


Fig. 14. Modeling curves corresponding to the objects of Fig. 8. (a) Modeling curves in space. (b) Projection of the modeling curves in (a) on the horizontal plane.

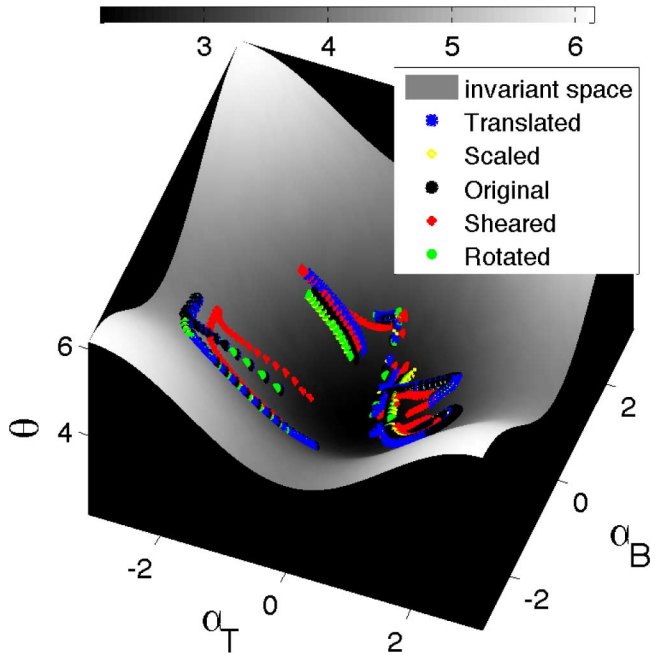


Fig. 15. Three-dimensional view of invariant traces for curves in Fig. 14.

primitive geometry, we mean that the corresponding topological graph is just one edge.

*1) Invariance to Pose:* As noted earlier, given that the shape of an object remains unaltered when subjected to a similarity transform, we require a geometric descriptor to be strictly and completely invariant to similarity transforms. To demonstrate the in-

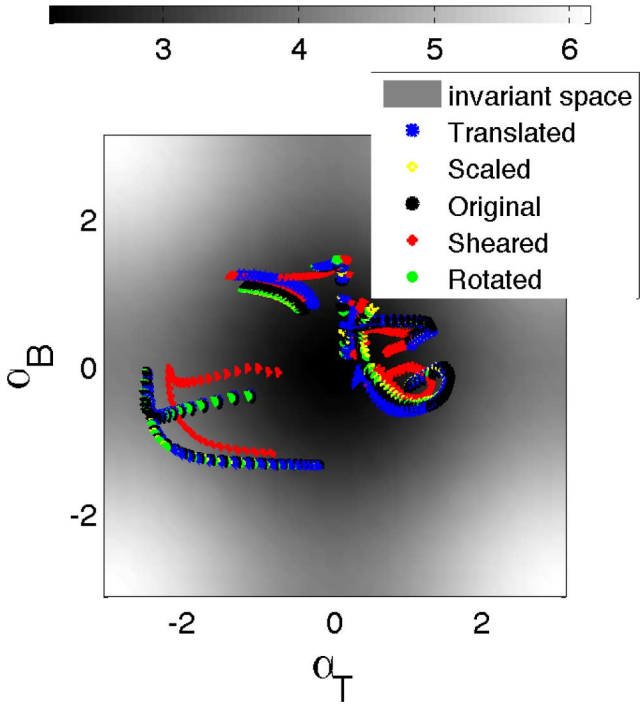


Fig. 16. Two-dimensional view of invariant traces for curves in Fig. 14.

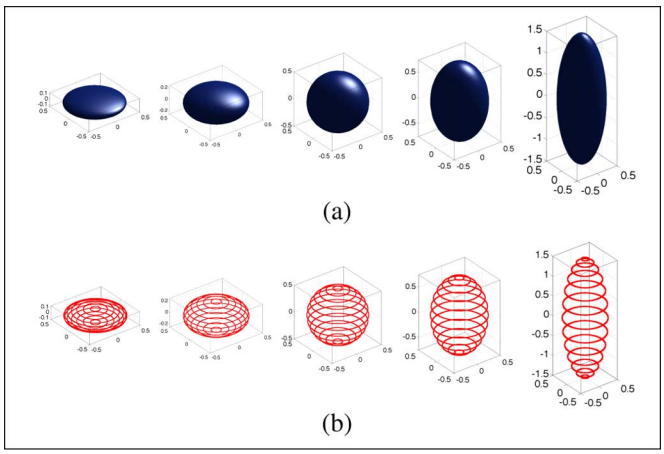


Fig. 17. Comparison of the geometry of five deformed spheres; (a) shows the five considered shapes and (b) shows the corresponding spatial modeling curves.

variance of a GGF to isometries by way of geometry modeling, we carry out the following experiment. Starting with the shape in Fig. 13(a), we apply each of the following transformations to it: (b) rotation, (c) scaling, (d) shearing, and (e) translation. In Fig. 14(a), we present the resulting five modeling curves that correspond to each shape of Fig. 13. To better visualize the differences of the curves in $\mathbb{R}^3$, we propose to project them on the plane as shown in Fig. 14(b). We note that all the modeling curves show, up to a similarity transform, a similar variation to that of the curve in black corresponding to the initial shape. This experimental result is consistent with the results of Appendix A. We say that two shapes are geometrically identical if their modeling curves are identical up to a similarity transform. For this reason, we use the representation of Section IV-B where the effects of similarity transforms are eliminated and all traces corresponding

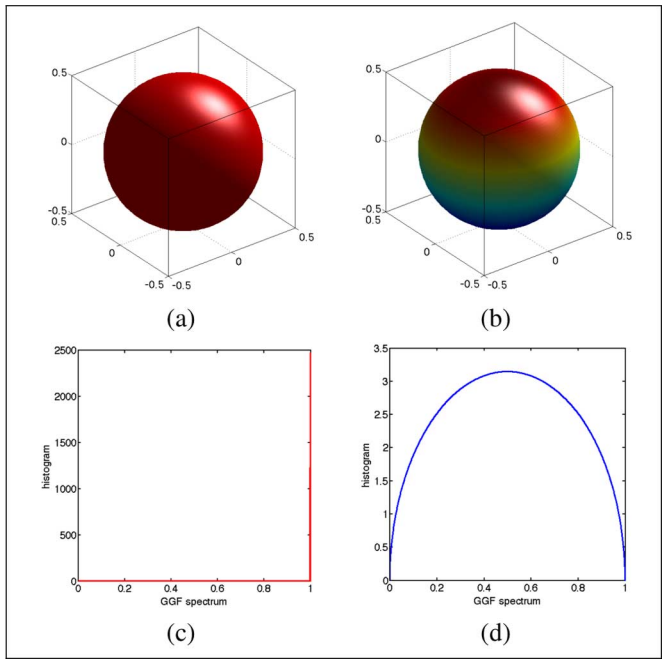


Fig. 18. Invariance to pose. The original object represented in (a) is subjected to: (b) a rotation transform, (c) a scaling transform, (d) a shearing transform and in (e) to a translation. (Best visualized in color).

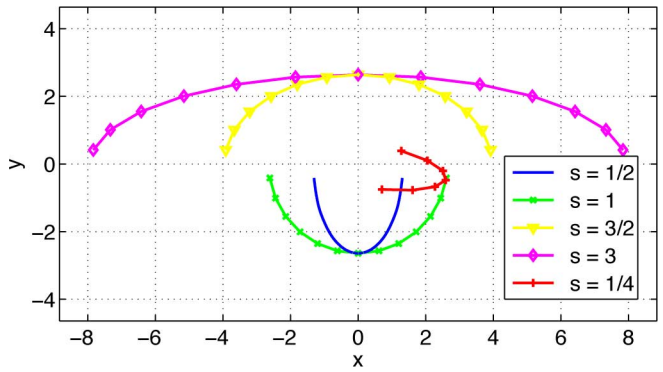


Fig. 19. Analysis of the effect of shearing transforms on the modeling curves.

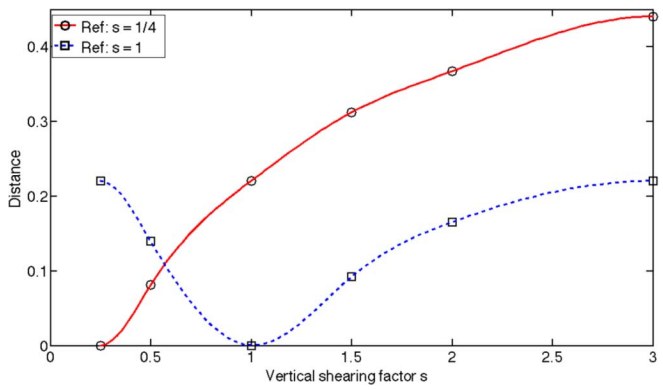


Fig. 20. Analysis of the effect of shearing transforms on the modeling curves.

to the modeling curves are registered. Identical geometries will hence see their traces fully overlap. We present the traces corresponding to this experiment in Fig. 15. We show the top view of these traces in Fig. 16. These traces are, by definition, invariant to

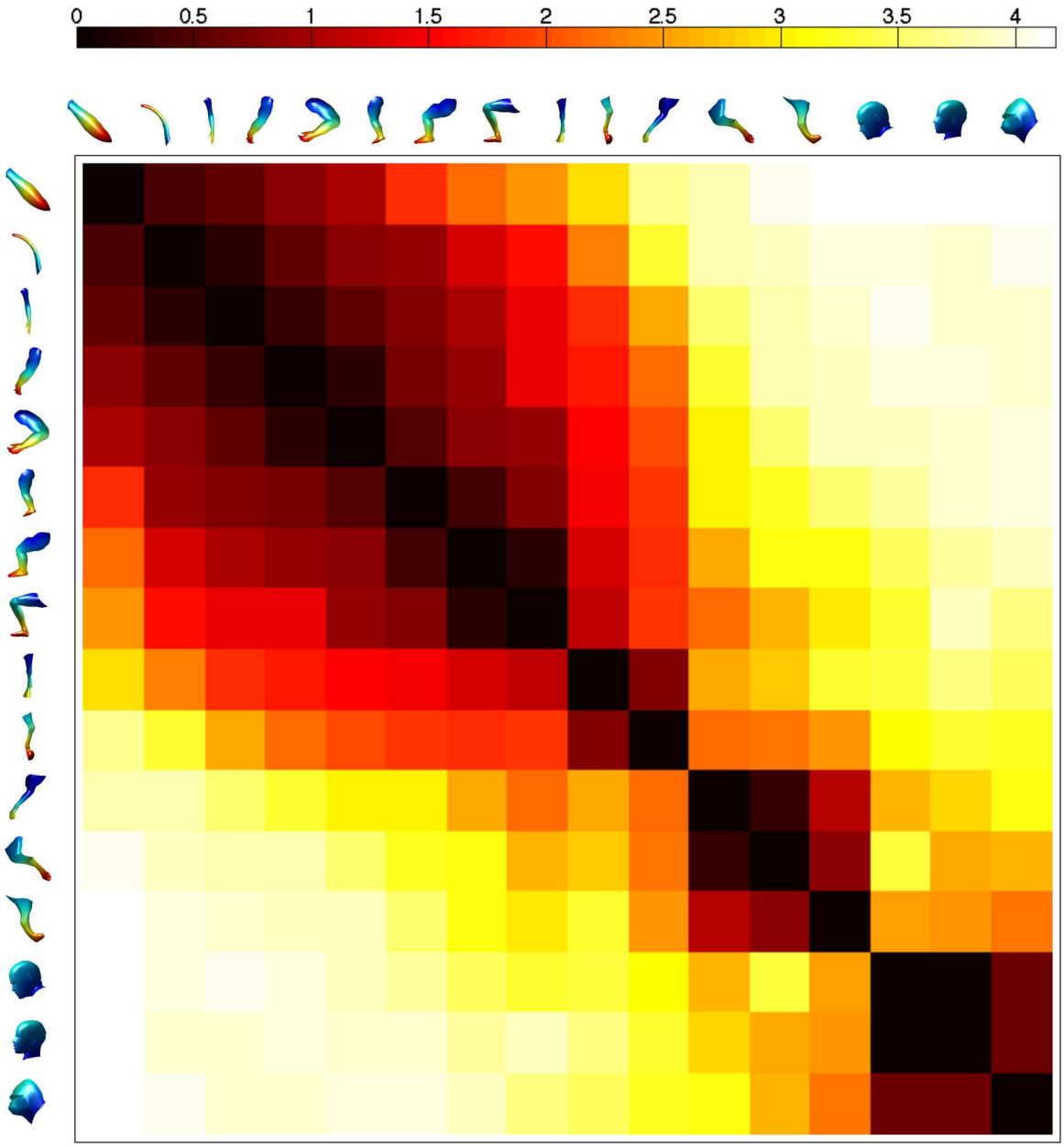


Fig. 21. Matching and comparison of the geometry of mono-cardinality subsurfaces.

all similarity transforms. We thus expect to see the result of Fig. 16, where all the traces overlap except for the one corresponding to the shearing transform; moreover, we find that the distance $\mathbb{D}$ [as defined in (19)] between the original shape and the sheared one is equal to 4.65 while the distance of other shapes away from the original one is between 0.08 and 0.29. Practically, we do not find a null dissimilarity between geometrically similar shapes because of slight differences due to approximations by sampling and the resulting Whitney embeddings.

*2) Progressive Deformation:* In order to analyze the progression of the distance $\mathbb{D}$, as a result of progressively deforming a primitive shape, we use the first ellipsoid starting from left in Fig. 17(a). This ellipsoid is defined by the following equation:

$$\frac{(x-x_0)^2}{(r_x)^2}+\frac{(y-y_0)^2}{(r_y)^2}+\frac{(z-z_0)^2}{(s\times r_z)^2}=1 \qquad (20)$$

with $(x_0,y_0,z_0)=(0,0,0)$, $(r_x,r_y,r_z)=((1/2),(1/2),(1/2))$, and $s=(1/4)$.

Each time, we apply a vertical shearing transform defined by the matrix $T(s)=\begin{pmatrix}1&0&0\\0&1&0\\0&0&s\end{pmatrix}$, $s$ being the shearing factor. We vary $s$ from $(1/4)$ to 3. We denote the resulting ellipsoid for a given $s$ by $\mathcal{E}(s)$. We note that $\mathcal{E}(1)$ is the 2-D sphere centered at the origin (0, 0, 0) with a radius equal to $(1/2)$. Before proceeding with the analysis of the present experiment, we have to answer a very important question that arises when considering singular shapes such as spheres. We first recall that we only talk about a Morse function when we ensure that all critical points are nondegenerate; thus, the GGF on a spherical shape is not a Morse function. Our proposed solution is to slightly disturb such a singular shape. For a spherical shape for instance, we

may disconnect a polar point from other points. As illustrated in Fig. 18, the distribution of the GGF on a spherical surface quickly changes from a simple Dirac function to the distribution shown in Fig. 18(d).

We apply this same perturbation technique to all the shapes in Fig. 17(a), and extract a modeling curve for each set of iso-geodesic curves in Fig. 17(b). Fig. 19 illustrates the resulting modeling curves. Our first observation is that these curves are planar, i.e., in $\mathbb{R}^2$, while the proposed Whitney modeling technique is in $\mathbb{R}^3$. This is due to the simplicity of the evolution of the iso-geodesic curves. Very briefly, we state that more variations imply more dimensions.

Focussing on this important aspect of predicting and understanding the modeling curves constitutes a future research direction. Indeed, the present experiment and its results lead to further investigations toward defining the applicability and limitations of the strong Whitney embedding versus the easy Whitney embedding theorem.[5]

Our choice of a simple progressive vertical shearing transform is motivated by two points: first, applying a simple directional geometric deformation, and second, being able to quantitatively describe this deformation. In the present example we use the shearing factor $s$ for this quantification; hence, we are able to visualize the variation of $\mathbb{D}$ versus $s$; thus, the red full curve in Fig. 20 shows the smooth evolution of the distance between $\mathcal{E}(1/4)$ and other ellipsoids with $(1/4) < s \leqslant 3$. Taking a sphere as the reference, i.e., $\mathcal{E}(1)$, we may see the effect of the vertical deformation in the two directions $s < 1$ and $s > 1$. The resulting distance curve is illustrated in Fig. 20 with a dotted blue line. We note that the distance $\mathbb{D}$ follows an exponential behavior as it starts slowing down for large values of $\Delta s$. One may explain this tendency by referring back to the human perception. In fact, looking at Fig. 17(a), we may classify these ellipsoids into two categories: category 1, corresponding to $s < 1$; and category 2, corresponding to $s > 1$, the sphere $(s = 1)$ representing the transition point. We then may say that when an ellipsoid is deformed to be away from its category, the distance $\mathbb{D}$ is relatively high, but once it reaches a new category, additional deformations in the same direction will only add slight distances. We find, for instance, that $\mathbb{D}(\mathcal{E}(2), \mathcal{E}(3)) = 0.045$ while $\mathbb{D}(\mathcal{E}(0.5), \mathcal{E}(1.5)) = 0.22$, that is about 5 times the first distance and for the same $\Delta s$. The present result constitutes an important step in understanding the geometry of shapes, and translating the human perception of geometry.

*3) Mono-Cardinality Subsurfaces:* In this experiment we continue our observation and analysis of mono-cardinality subsurfaces, but this time we consider more complex shapes found in real-world objects. We thus compare selected parts that constitute the edges of the *squigraphs* extracted for the data sets used in Section V-A.

We summarize our comparison results with the confusion matrix in Fig. 21. We note that when legs are bent, the modeling curves are still able to detect a difference between stretched and bent legs. This phenomenon is equivalent to the example of Section IV-B where we illustrated how the modeling curves, and *squigraphs* in general, are able to detect an inflection point. Depending on the application, one might think of bent and stretched legs (or arms) as being the same. In this case, we note that, while modeling curves are still able to be lenient on the effect of one inflection point, we recommend for simplicity and efficiency to directly use the distribution of the GGF along each part.

[5]Indeed, while the easy Whitney embedding theorem allows embedding an n-dimensional Hausdorff manifold into $\mathbb{R}^{2n+1}$, the strong Whitney embedding allows going lower and defining an embedding in $\mathbb{R}^{2n}$ [17].

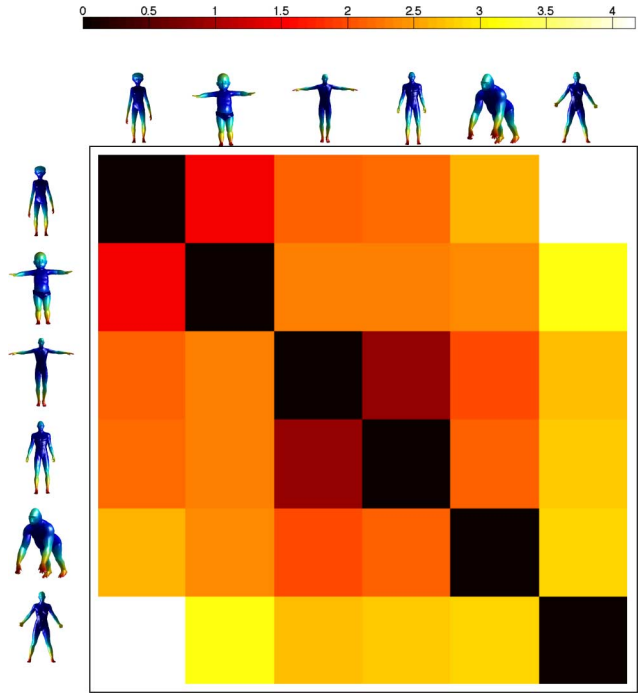


Fig. 22. Comparison and matching of 6 different bipedal subjects.

### C. Shape Matching

The synthesis of the distances between different mono-cardinality subsurfaces provides a global distance for complex shapes as given by (19). We present a couple of relevant examples of confusion matrices for different classes and subclasses of 3-D shapes. In Fig. 22, we note the power of the *squigraph* technique in differentiating between objects that are topologically similar, but belonging to distinct object classes. Intuitively, one might expect the male subject of column 3 (or similarly the one of column 4) to be more similar to the female subject of column 6. To understand this distance, that is relatively higher than expected, we need to refer to the respective decompositions of the two subjects into primitives. The two subjects in question are the two first subjects (starting from the left), male and female, illustrated in Fig. 2. The partitioning is shown in Fig. 2(c). We notice that, in contrast with the male subject, the arm part on the female subject extends beyond the shoulder. This in turn affects the part by part comparison, as the considered primitive comparison operation changes. Consequently, the overall distance gets affected. This ability to distinguish between shapes with fine geometric differences illustrates the core concept of squigraphs.

The results of Fig. 22 prove the importance of the shape partitioning step. The partitioning is governed by the choice of the

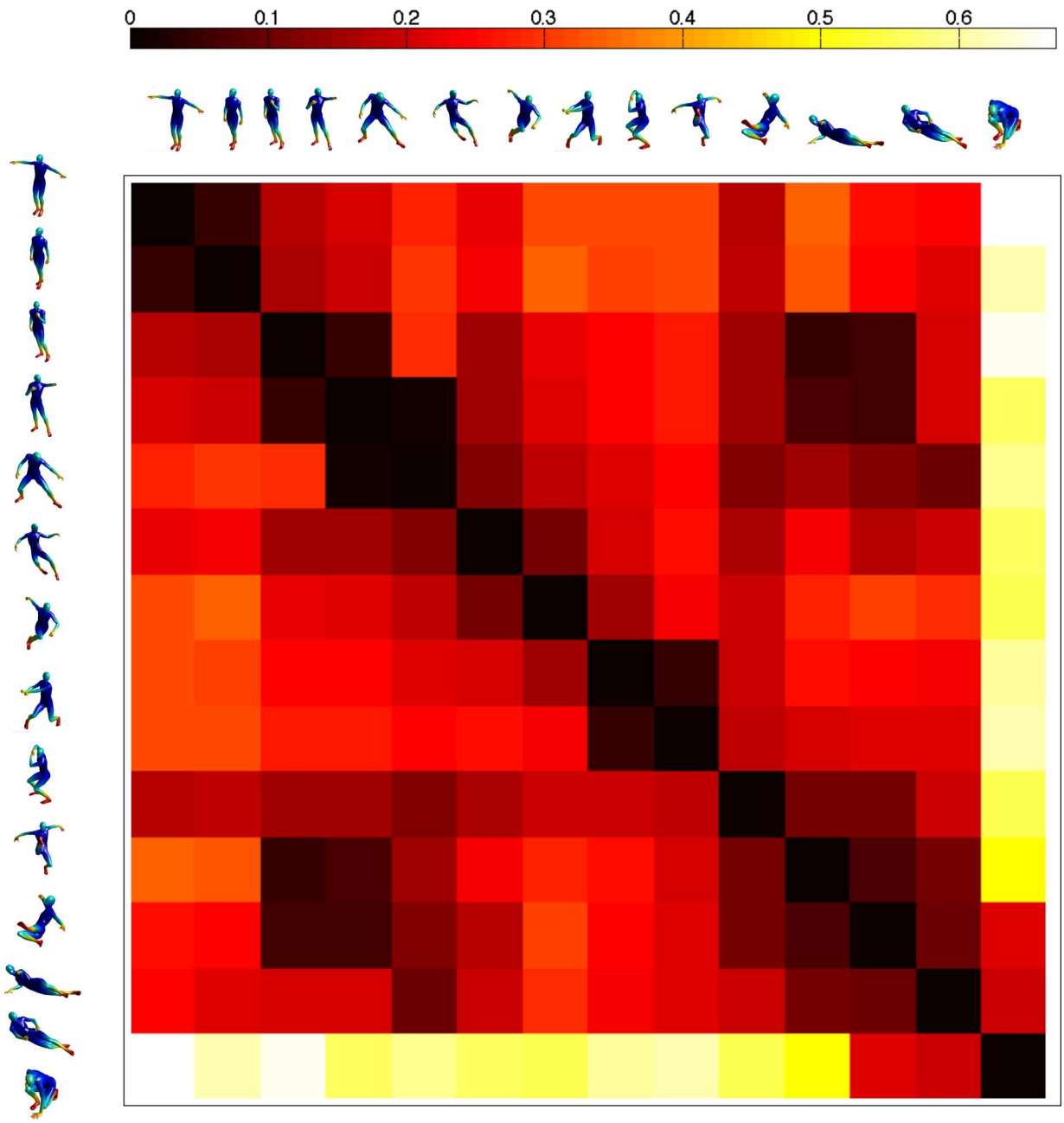


Fig. 23. Comparison and matching of the 14 different poses for the same subject.

Morse function, the GGF in our experiments, and how it translates the topological and geometric features of a shape. We recall that a partitioning happens wherever there is a change in the cardinality of the level curves of the Morse function.

In Fig. 23, we present the result of comparing the same object/subject, but in different poses. Our first comment is that all distances in this experiment are low in comparison with those of Fig. 22. This means that within-class distances are lower than distances between classes. This observation indicates that the geometry of shapes from the same class is very similar, causing consistent partitioning results. So what is behind the differences between poses? The answer is in the changes that occur on primitive shapes. The Whitney embedding representation of primitives being only invariant to rigid transforms, all nonrigid transforms (e.g., bending transforms) are now detected. This explains the relatively large distance between pose 1 and pose 14, or also the distinction between poses 2 and 3 because of one bent arm.

### D. Robustness Evaluation

For the practical applicability of the modeling space curves and the final *squigraphs*, it is important to evaluate their robustness to both noise and object discrete decimation.

*1) Robustness to Noise:* As for any practical problem, the measurements, when scanning 3-D models, contain additive noise. The secant-based method (described earlier), being directly dependent on the data, raises natural concern about the level of accuracy of the modeling curves in presence of noisy measurements. For testing purposes, we add Gaussian

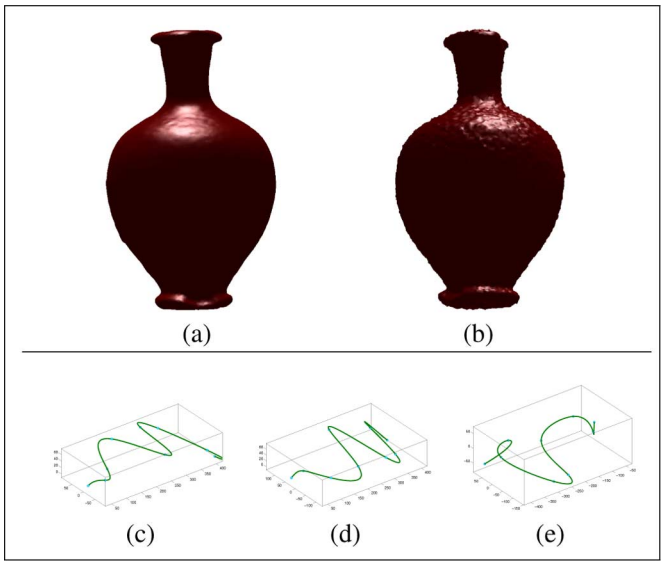


Fig. 24. Robustness to noise by short secants filtering.

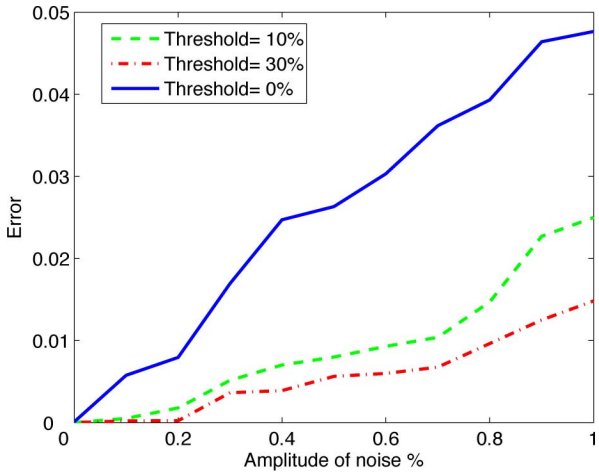


Fig. 25. Secants filtering with different thresholds.

noise with an amplitude ranging between 0 to 1% of the shape bounding radius for each considered object. Fig. 24(a) and (b) illustrate the object "Vase" with and without additive noise. In Fig. 24(e), we observe the impact of noise on the modeling curve. The dissimilarity score between the initial shape "Vase" and its noisy version is of 3.08. This basically indicates that the two modeling curves are very different and may induce an erroneous recognition result. Broomhead and Kirby [20] propose a solution to alleviate the effect of noise on embeddings. They show that the shortest secants induce the most severe distortion. We propose, as a result, to filter the shortest secants prior to applying the LTMADS algorithm. We test the effect of filtering out the short secants where the threshold is a fraction of the longest secant. Fig. 25 illustrates the result of 250 Monte Carlo simulations. It is clear that the errors due to noise are reduced after filtering, with a more dramatic impact for larger thresholds.

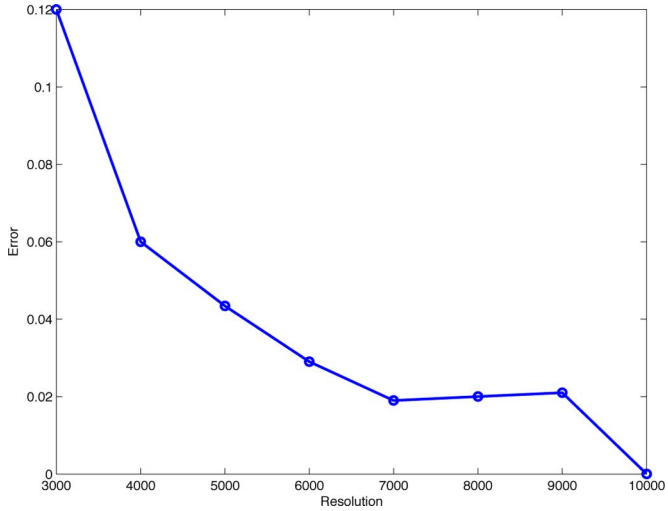


Fig. 26. Robustness to decimation.

*2) Robustness to Decimation:* The resolution of a 3-D object measurement/scanning may vary with applications, and it is, hence, important to evaluate our proposed geometric modeling in presence of such variations. To that end, we consider an object "Frog" to assess the robustness of the modeling to decimation. Taking the highest resolution, of 10000 vertices, as a reference, we measure the dissimilarity induced by a progressive decrease in resolution for object "Frog". We illustrate this experiment in Fig. 26. As explained in [8], using the GGF, we may assign a particular resolution, to each shape, referred to as a *characteristic resolution*. By definition, the characteristic resolution corresponds to the lowest number of vertices able to accurately represent a considered shape. For the shape "Frog", we find that the characteristic resolution is about 5000 points. Analyzing the results of Fig. 26, we may conclude that for "Frog", our modeling is accurate for resolutions greater or equal to the characteristic resolution of 5000 points. Thus, our geometric modeling is consistent and nearly invariant to decimation.

## VI. Conclusion

We presented a novel and effective geometric modeling technique which significantly reduces a 3-D shape representation to a *squigraph*. Thanks to their topological and geometric natures, *squigraphs* provide multiple levels of discrimination between shapes. A property that is important in classification and recognition problems. Furthermore, the choice of a geodesic-based Morse function ensures *squigraphs* to be suitable for the representation of articulated shapes. Our experimental results are encouraging to warrant further study and more expanded applications such as describing complex scenes with moving subjects. Many interesting questions arose from this work, and remain to be investigated.

- How to formalize the interactions between topology and geometry, and how do they affect each other in the extraction of a squigraph?
- Is there a need to define a new Morse function that not only incorporates the desired invariance properties, but also the human perception of shapes?

## APPENDIX
## PROOF OF EQUIVALENCE OF MODELING CURVES UP TO A SIMILARITY TRANSFORM

If a 3-D shape is subjected to a similarity transform, then each point $\mathbf{V}_j^i$ in $\mathbb{R}^3$ defined by the coordinates $\left(x_j^i, y_j^i, z_j^i\right)$ is transformed as follows:

$$\mathbf{V'}_j^i = \alpha \mathbf{Q} \mathbf{V}_j^i + \mathbf{K} \tag{21}$$

where $\alpha$ is a scaling factor, $\mathbf{Q}$ is a $(3 \times 3)$ unitary matrix, i.e., $\mathbf{Q}\mathbf{Q}^T = \mathbf{I}_3$, and $\mathbf{K}$ is a $(3 \times 1)$ translation vector. Considering the construction in (5) and the transform in (21), each point $\mathbf{V}_i$ in $\mathbb{R}^{3M}$ is transformed by

$$\mathbf{V}'_i = \alpha \underline{\mathbf{Q}} \cdot \mathbf{V}_i + \underline{\mathbf{K}} \tag{22}$$

with

$$\underline{\mathbf{Q}} = \begin{bmatrix} \mathbf{Q} & & & \\ & \mathbf{Q} & & \\ & & \ddots & \\ & & & \mathbf{Q} \end{bmatrix}, \text{ and } \underline{\mathbf{K}} = \begin{bmatrix} \mathbf{K} \\ \mathbf{K} \\ \vdots \\ \mathbf{K} \end{bmatrix}.$$

The question of concern is to find the transform applied to a modeling curve when the 3-D shape it originates from is subjected to a similarity transform. If $\mathbf{P}$ is defined by (9), we may define $\mathbf{P'}$ as follows:

$$\hat{\mathbf{P}}' = \arg\min \left[ - \min_{i=1,\ldots,L} \left\| \mathbf{P}^T \mathbf{\Psi}'_i \right\|_2 \right].$$

Since the new secants $\mathbf{\Psi}'_i$, $i = 1, \ldots, L$, result from the same (22) as $\mathbf{V}'_i$, we conclude that $\mathbf{P'}$ is directly related to $\mathbf{P}$ through a permutation (or a rotation) matrix. In other words: $\mathbf{P}' = \underline{\mathbf{Q}}\mathbf{P}\mathbf{U}$, where $\mathbf{U}\mathbf{U}^T = \mathbf{I}_3$; thus, we may write

$$\begin{aligned} \mathbf{W}' &= \mathbf{P}'^T \cdot \mathbf{V}' \\ &= \left(\underline{\mathbf{Q}}\mathbf{P}\mathbf{U}\right)^T \cdot \left(\alpha \underline{\mathbf{Q}}\mathbf{V} + \underline{\mathbf{K}}\right) \\ &= \alpha \left(\mathbf{P}\mathbf{U}\right)^T \cdot \underline{\mathbf{Q}}^T \cdot \underline{\mathbf{Q}}\mathbf{V} + \left(\underline{\mathbf{Q}}\mathbf{P}\mathbf{U}\right)^T \cdot \underline{\mathbf{K}} \\ &= \alpha \mathbf{U}^T \cdot \mathbf{P}^T \mathbf{V} + \mathbf{L} \\ &= \alpha \mathbf{U}^T \cdot \mathbf{W} + \mathbf{L}. \end{aligned} \tag{23}$$

From (23), we conclude that if a shape in 3-D is subjected to a similarity transform (translation, rotation, scaling, or a combination thereof), then its modeling curve in 3-D is subjected to the same group of transforms.

## ACKNOWLEDGMENT

The authors would like to thank D. Dreisigmeyer for introducing them to Whitney embedding which they subsequently exploited in 3-D shape modeling, as well as for graciously providing the LTMADS code. The authors would also like to thank T. Tung and F. Schmitt for providing the aMRG executable, as well as S. Morgan, K. Vixie, and the anonymous reviewers for their thorough review of the present paper and for their valuable comments and suggestions.

## REFERENCES

[1] J. W. H. Tangelder and R. C. Veltkamp, "A survey of content based 3D shape retrieval methods," *Multimedia Tools Appl.*, vol. 39, no. 3, pp. 441–471, Sep. 2008.
[2] V. Jain and H. Zhang, "Robust 3D shape correspondence in the spectral domain," in *Proc. Shape Model. Int.*, 2006, pp. 118–129.
[3] M. Yu, I. Atmosukarto, W. K. Leow, Z. Huang, and R. Xu, "3D model retrieval with morphing-based geometric and topological feature maps," in *Proc. IEEE Computer Society Conference on Computer Vision and Pattern Recognition*, 2003, vol. 2, pp. II-656–61.
[4] T. Tung and F. Schmitt, "The augmented multiresolution Reeb graph approach for content-based retrieval of 3D shapes," *Int. J. Shape Model.*, vol. 11, no. 1, pp. 91–120, 2005.
[5] S. Baloch, H. Krim, I. Kogan, and D. Zenkov, "Rotation invariant topology coding of 2D and 3D objects using Morse theory," in *Proc. IEEE Int. Conf. Image Processing*, 2005, pp. 796–799.
[6] G. Reeb, *Sur les Points Singuliers D'une Forme de Pfaff Complètement Intégrable ou D'une Fonction Numérique*. Paris, France: Comptes rendus de l'Académie des sciences, 1946, pp. 847–849.
[7] Y. Shinagawa, T. L. Kunii, A. G. Belyaev, and T. Tsukioka, "Shape modeling and shape analysis based on singularities," *Int. J. Shape Model.*, vol. 2, pp. 85–102, Mar. 1996.
[8] D. Aouada, S. Feng, and H. Krim, "Statistical analysis of the global geodesic function for 3D object classification," presented at the 32nd IEEE Int. Conf. Acoustics Speech and Signal Processing, 2007.
[9] D. Aouada and H. Krim, "3D object recognition using fully intrinsic skeletal models," *Proc. SPIE*, vol. 6814, no. 8, 2008.
[10] D. Aouada, D. W. Dreisigmeyer, and H. Krim, "Geometric modeling of rigid and non-rigid 3D shapes using the global geodesic function," presented at the IEEE Computer Society Conf. Computer Vision and Pattern Recognition Workshops, 2008.
[11] M. Hilaga, Y. Shinagawa, T. Kohmura, and T. L. Kunii, "Topology matching for fully automatic similarity estimation of 3D shapes," in *Proc. SIGGRAPH*, Aug. 2001, pp. 203–212.
[12] A. B. Hamza and H. Krim, "Geodesic matching of triangulated surfaces," *IEEE Trans. Image Process.*, vol. 15, no. 8, pp. 2249–2258, Aug. 2006.
[13] J. Zhang, K. Siddiqi, D. Macrini, A. Shokoufandeh, and S. Dickinson, "Retrieving articulated 3-D models using medial surfaces and their graph spectra," in *Proc. EMMCVPR*, 2005, vol. LNCS 3757, pp. 285–300.
[14] A. Verroust and F. Lazarus, "Extracting skeletal curves from 3D scattered data," in *Proc. Shape Modeling and Applications*, pp. 194–201.
[15] J. Milnor, *Morse Theory*. Princeton, NJ: Princeton Univ. Press, 1963.
[16] A. T. Fomenko and T. L. Kunii, *Topological Modeling for Visualization*. New York: Springer-Verlag, 1997.
[17] M. W. Hirsh, *Differential Topology, Graduate Texts in Mathematics*. New York: Springer-Verlag, 1976, vol. 33.
[18] X. Ni, M. Garland, and J. C. Hart, "Fair Morse functions for extracting the topological structure of a surface mesh," *ACM Trans. Graph.*, pp. 613–622, 2004.
[19] D. S. Broomhead and M. Kirby, "New approach for dimensionality reduction: Theory and algorithms," *SIAM J. Appl. Math.*, vol. 60, no. 6, pp. 2114–214, 2000.
[20] D. S. Broomhead and M. J. Kirby, "The Whitney reduction network: A method for computing autoassociative graphs," *Neural Comput.*, vol. 13, pp. 2595–2616, 2001.
[21] D. W. Dreisigmeyer, Direct Search Algorithms Over Riemannian Manifolds 2007 [Online]. Available: http://ddma.lanl.gov/Documents/publications/dreisigm-2007-direct.pdf
[22] D. Aouada and H. Krim, "Meaningful 3D shape partitioning using Morse functions," presented at the 16th IEEE Int. Conf. Image Processing 2009.
[23] P. N. Klein, T. B. Sebastian, and B. B. Kimia, "Shape matching using edit-distance: An implementation," in *Proc. 12th Annu. Symp. Discrete Algorithms*, 2001, pp. 781–790.
[24] I. Biederman, "Recognition-by-components: A theory of human image understanding," *Psych. Rev.*, vol. 94, pp. 115–147, 1987.
[25] S. P. Morgan and K. R. Vixie, "L1TV computes the flat norm for boundaries," *Abstract Appl. Anal.*, vol. 2007, pp. 14–14, 2007.

[26] F. Morgan, *Geometric Measure Theory: A Beginner's Guide*, 3rd ed. New York: Academic, 2000.
[27] M. Vaillant and J. Glaunès, "Surface matching via currents," in *Proc. Information Processing in Medical Imaging*, 2005, vol. 3565, Springer Lecture Notes in Computer Science.
[28] J. Lin, "Divergence measures based on Shannon entropy," *IEEE Trans. Inf. Theory*, vol. 37, pp. 145–151, 1991.
[29] Y. He, A. Ben Hamza, and H. Krim, "A generalized divergence measure registration for robust image registration," *IEEE Trans. Signal Process.*, vol. 51, pp. 1211–1220, 2003.
[30] R. Osada, T. Funkhouser, B. Chazelle, and D. Dobkin, "Shape distributions," *ACM Trans. Graph.*, vol. 21, pp. 807–832, 2002.
[31] P. Shilane, P. Min, M. Kazhdan, and T. Funkhouser, "The Princeton shape benchmark," presented at the Shape Modeling Int., Genova, Italy, Jun. 2004.
[32] A. M. Bronstein, M. M. Bronstein, and R. Kimmel, *Numerical Geometry of Non-Rigid Shapes*. New York: Springer Verlag, 2007.
[33] A. M. Bronstein, M. M. Bronstein, and R. Kimmel, "Calculus of non-rigid surfaces for geometry and texture manipulation," *IEEE Trans. Vis. Comput. Graph.*, vol. 13/5, pp. 902–913, 2007.
[34] A. M. Bronstein, M. M. Bronstein, and R. Kimmel, "Efficient computation of isometry-invariant distances between surfaces," *SIAM J. Sci. Comput.*, vol. 28/5, pp. 1812–1836, 2006.
[35] J. Feldman and M. Singh, "Information along contours and object boundaries," *Psych. Rev.*, vol. 112, no. 1, pp. 243–252, 2005.
[36] C. Shannon, "A mathematical theory of communications," *Bell Syst. Tech. J.*, vol. 27, pp. 379–423, 1948.
[37] K. Kazhdan and T. Funkhouser, "Harmonic 3D shape matching," *SIGGRAPH Tech. Sketches*, pp. 191–191, 2002.

**Djamila Aouada** (M'05) was born in Blida, Algeria, on November 10, 1982. She received the State Engineering degree (Ingéniorat d'État) in electronics in June 2005, from the École Nationale Polytechnique (ENP), Algiers, Algeria, and the Ph.D. degree in electrical engineering in May 2009 from North Carolina State University (NCSU), Raleigh.

From June to August 2007, she participated in the data sciences summer school at Los Alamos National Laboratory (LANL), Los Alamos, NM, as part of the Geometric Measure Theory group (GMT). From July to September 2008, she worked as a consultant for Alcatel-Lucent Bell Laboratories, Murray Hill, NJ. She is currently a Research Associate at the Interdisciplinary Centre for Security, Reliability and Trust (SnT) in Luxembourg. Her research interests span the areas of signal and image processing, computer vision, pattern recognition, and data modeling.

Dr. Aouada is member of the Society of Women Engineers (SWE) and the Eta Kappa Nu honor society (HKN).

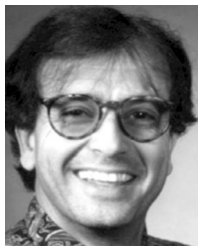

**Hamid Krim** (F'08) received the B.Sc., M.Sc., and Ph.D. degrees from the University of Washington and Northeastern University, respectively.

He was a Member of Technical Staff at AT&T Bell Labs, where he has conducted research and development in the areas of telephony and digital communication systems/subsystems. Following an NSF postdoctoral fellowship at the Foreign Centers of Excellence, LSS/University of Orsay, Paris, France, he joined the Laboratory for Information and Decision Systems, Massachusetts Institute of Technology, Cambridge, as a Research Scientist and where he was performing and supervising research. He has held several visiting positions in different labs in the U.S. and Europe, and is presently a Professor of electrical engineering in the ECE Department, North Carolina State University, Raleigh, NC, leading the Vision, Information, and Statistical Signal Theories and Applications Group. His Research interests are in statistical signal and image analysis and mathematical modeling with a keen emphasis on applied problems in classification and recognition.